Aqueous phase hydrogenolysis of glycerol over Ni/Al-Fe catalysts without external hydrogen addition

R. Raso, L. García*, J. Ruíz, M. Oliva, J. Arauzo

Thermochemical Processes Group (GPT), Aragon Institute of Engineering Research (I3A), Universidad de Zaragoza, Mariano Esquillor S/N, 50018 Zaragoza, Spain

Abstract

The present work studied the aqueous phase hydrogenolysis (APH) of glycerol (a by-product of biodiesel manufacturing) without external hydrogen addition to produce value-added products. A series of catalysts based on 28 molar % of Ni were prepared through co-precipitation by changing the Al/Fe molar ratio. The calcined and used catalysts were characterized by several techniques (ICP-OES, N_2-physisorption, XRD, H_2-TPR, NH_3-TPD, FESEM and STEM). This work examines the effects of the molar ratio of Al/Fe on the physicochemical characteristics of Ni/Al-Fe catalysts and during the APH of glycerol. All the catalysts showed low carbon yields to gases and high carbon yields to liquid products, mainly 1,2-propanediol, acetol and ethylene glycol. Ni/Al_3Fe_1 catalyst gave the best performance in the APH of glycerol: the highest glycerol conversion (42.31 %), carbon yield to gases (6.57 %) and carbon yield to liquids (30.45%). 1,2-propanediol was the liquid product with the highest carbon selectivity (70.89%).

Keywords: glycerol, in situ hydrogen, catalytic conversion, fixed bed reactor

*Corresponding author: E-mail address: luciag@unizar.es (L. García).

1. Introduction

Environmental contamination and petroleum depletion have encouraged researchers to find sustainable energy alternatives. In this context, the use of biomass as a renewable organic resource is an alternative to oil. Several value-added products and fuels can be obtained from biomass such as biogas, bio-oil, bioethanol, as well as biodiesel, which has had greater increases in production than other biofuels for the last decade [1, 2]. Biodiesel (fatty acid methyl esters, FAME) is biodegradable, renewable and clean burning. It has a high flash point, better viscosity and a caloric power similar to that of fossil fuels [3]. Biodiesel is currently produced by the transesterification of triglycerides (vegetable oils, animal fats and waste oils) using an alcohol (methanol or ethanol) in the presence of a catalyst, the main by-product being glycerol [1, 4]. Nowadays, the high production of biodiesel leads to a large surplus of glycerol. Around 1 ton of glycerol is generated for every 10 tons of biodiesel. In light of this, several processes have been investigated in order to valorise glycerol [5-8]. It is now used in various industries, mainly in cosmetics, pharmaceuticals and food, and can be used as a humectant in sweets, cakes, meats and cheeses, plasticizers, antifreezes and solvents, among others [6, 9, 10]. It is also one of the top 12 building block chemicals that can be transformed into value-added products in the bio-refinery field [11]. The use of glycerol has several advantages. On the one hand, the benefits of its valorisation improve the economic viability of biodiesel industries and, on the other hand, the generation of waste and its treatment are avoided [6].

In the bio-refinery context, a promising valorisation strategy to obtain value-added chemicals from glycerol is aqueous phase hydrogenolysis without external hydrogen addition (APH w/o H_2). APH w/o H_2 is a catalytic process performed at moderate pressures around 34 bar and quite low temperatures around 227 ºC, allowing the

production of gases and liquids from a renewable feedstock. In addition, it does not need an external supply of H_2, like aqueous phase reforming (APR) of glycerol [5, 7], so it is a less expensive and safer process than conventional aqueous phase hydrogenolysis. Overall, high H_2 pressure is necessary to obtain value-added products such as 1,2-propanediol, acetol and ethylene glycol during the APH of glycerol [8]. Fortunately, in situ H_2 production and its simultaneous consumption in the APH of glycerol could solve most of the drawbacks inherent in the use of molecular H_2 as feed [12, 13]. The challenge of this work is to obtain value-added products from glycerol such as 1,2-propanediol, acetol, ethylene glycol and so forth through APH with in situ H_2 formation. Other benefits of this process are that the feed does not require previous vaporization and the feeding is continuous, which is useful due to the greater production potential on an industrial scale. The review of Martin et al. [9] reports on glycerol hydrogenolysis using in situ generated H_2 by APR and catalytic transfer hydrogenation using hydrogen donor molecules. In addition, Yfanti et al. [14] refer to the hydrodeoxygenation of glycerol with in situ H_2 formation by APR from the alcohol present in crude glycerol.

1,2-propanediol, also called propylene glycol, is an important chemical commodity mainly used in unsaturated polyester resins, functional fluids (for antifreeze, de-icing, and heat transfer), foods, cosmetics, pharmaceuticals, liquid detergents, paints and animal feed, among others [15]. Ethylene glycol is an important bulk chemical with applications in antifreeze and as a raw material for the production of polyester fibres [16]. Acetol (hydroxyacetone) is used to obtain products such as propylene glycol, acrolein, acetone, propionaldehyde and furan derivatives. It is also utilized in the food, cosmetics and textile industries [17].

It is known that APH and APR of glycerol are catalytic processes, which can be operated under similar conditions (200-250 ºC and 20-50 bar). By coupling both reactions, APR may serve as an H_2 source for APH [18]. Many works have been published on APR and/or APH of glycerol for H_2 production, as well as for 1,2-propanediol and other value-added products, using a variety of catalysts. The catalysts used in the processes are based on noble metals such as Pt [14, 18-23], Ru [19, 22, 23], Pd [18], Rh [24] and transition metals such as Cu [8, 25] , Ni [5, 7, 16, 18, 25-30], Co [31] or Zr [32]. Some bimetallic catalysts such as Ni-Zr [32], Ni-La [33], Pt-Mn [20], Ni-Cu [13, 34], Pt-Ni [29], Cu-B [8] or Pt-Fe [35] have also been employed. They are supported on different oxides such as Al_2O_3, ZrO_2, SiO_2, MgO, CeO_2, TiO_2, Fe_3O_4, ZSM-5, H-beta, SBA-15 or activated carbon. Additionally, mixed oxide supports have been studied in these processes [14, 22, 27, 28]. Seretis and Tsiakaras [27] studied experimentally the APR and APH of glycerol in a batch reactor (V = 600 mL), using 65% Ni catalyst supported on SiO_2-Al_2O_3. The maximum H_2 yield (23.5%) was achieved with short reaction times (30 min) and a low glycerol concentration (1 wt.%) at 240 ºC, under low autogenous pressure. Conversely, a maximum propylene glycol yield (22%) was obtained after 4 h of reaction with a high glycerol concentration (10 wt.%) at 240 ºC, under high autogenous pressure. Bastan et al. [28] investigated the effect of Al, Mg and the Al/Mg ratio on the behaviour of 5 wt.% Ni catalysts in the production of H_2 through APR of glycerol in a fixed bed tubular reactor with 10 wt.% glycerol solution, a weight hourly space velocity (WHSV) of 2.45 h^{-1} at 250 ºC and 50 bar. The highest glycerol conversion (92%) and H_2 selectivity (76%) were attained with the catalyst 5 wt.% Ni/Al_2Mg_1, which was the highest Al/Mg ratio studied. It was demonstrated that the mixed oxide supports favoured the production of H_2 in comparison to 5 wt.% Ni/Al_2O_3 and 5 wt.% Ni/MgO catalysts, in the following order:

Ni/Al_2Mg_1 > Ni/Al_1Mg_1 > Ni/Al_1Mg_2 > Ni/Al_2O_3 > Ni/MgO. Yfanti et al. [14] reported the effect of the Fe content on the conversion of glycerol to 1,2-propanediol with in situ H_2 formation. The maximum glycerol conversion (93.8%) and 1,2-propanediol selectivity (51.5%) were achieved over the Fe richer catalyst ($Pt/Fe_2O_3(58)$-Al_2O_3) after 1 h of reaction time at 250 ºC, under 3.5 MPa N_2 and pre-reduction at 200 ºC. It was observed that the addition of Fe favours catalytic activity and selectivity for hydrogenolysis towards 1,2-PDO, as reported by Soares et al. [35].

Nickel-based catalysts are interesting materials for use in the APH of glycerol because of their high reactivity, accessibility and low price [29]. Furthermore, they have high activity for producing H_2 in situ, which is a benefit for the hydrogenation reaction, and Ni has the ability to break the C-C bond efficiently towards the production of ethylene glycol [25, 34]. According to reports in the literature [12, 13, 36], bifunctional catalysts are promising materials for glycerol hydrogenolysis, affecting its mechanism to obtain 1,2-propanediol, since they have acid sites as well as active metal. Acid sites favour dehydration of glycerol to acetol and then the hydrogenation of acetol to 1,2-propanediol is produced over metallic centres. Acid supports such as zeolites, alumina and silica-alumina have been used for this purpose [36].

With this background, this work studies the effects of the molar ratio of Al/Fe on the physicochemical characteristics of the catalysts based on Ni. The different Ni/Al-Fe catalysts were prepared by co-precipitation. To the best of our knowledge, the properties and the performance of these catalysts for the APH of glycerol as well as the APR of glycerol have not yet been investigated. However, the introduction of Fe in Ni/Al_2O_3 catalyst has been studied in others processes, for example in the production of H_2 through the decomposition of methane [37] and the obtaining of synthetic natural gas from CO hydrogenation [38], among others. The aim of this work was to analyse the

performance of these catalysts during the APH of glycerol to obtain value-added products in a continuous installation. The calcined and used catalysts were characterized using several techniques such as inductively coupled plasma optical emission spectrometry (ICP-OES), N_2-physisorption, X-ray diffraction (XRD), hydrogen temperature-programmed reduction (H_2-TPR), temperature-programmed desorption of ammonia (NH_3-TPD), field emission scanning electron microscopy (FESEM) and scanning transmission electron microscopy (STEM).

2. Experimental

2.1. Catalysts preparation

The different Ni/Al-Fe catalysts were prepared by the co-precipitation method with different Al/Fe molar ratios, but all of them containing a 28 molar % of Ni (the molar ratio Ni/(Ni + Al + Fe) constant at 28%). The molar ratio of Al/Fe was varied with values of 1/0, 3/1, 1/1, 1/3 and 0/1 and the samples were named Ni/Al, Ni/Al_3Fe_1, Ni/Al_1Fe_1, Ni/Al_1Fe_3 and Ni/Fe, respectively. Aluminium nitrate [$Al(NO_3)_3 \cdot 9H_2O$] (Fluka analytical, purity: ≥ 98.0 %), nickel nitrate [$Ni(NO_3)_2 \cdot 6H_2O$] (Sigma-Aldrich, purity: ≥ 97.0 %) and iron nitrate [$Fe(NO_3)_3 \cdot 9H_2O$] (Panreac, purity: ≥ 98.0 %) were used as metal precursors, while NH_4OH was employed as precipitant. The mixture of nitrates was dissolved in mili-Q water, heated to 40 ºC, and the temperature maintained at this value. The precipitant was added slowly to attain the precipitation pH value (pH = 7.8). Vigorous stirring was employed during the synthesis. The precipitates were filtered and washed with 400 mL of mili-Q water at 40 ºC. The catalyst-hydrated precursors were dried overnight at 105 ºC and then calcined at a final temperature of 500 ºC for 3 h in a furnace. The heating rate was very smooth while leading up to the final calcination temperature. Finally, the calcined samples were sieved to a mesh size

of 160 - 315 μm.

2.2 Catalysts characterization

The metal loadings in the calcined catalysts were measured by inductively coupled plasma optical emission spectrometry (ICP-OES) after microwave digestion of the samples in aqua regia. The equipment used was a Thermo Elemental IRIS Intrepid Radial with an automatic injector. Textural properties of the solids were obtained from the N_2 adsorption-desorption isotherms determined at 77 K using a Quantachrome instrument. Previously, the samples were outgassed at 300 ºC and 10^{-3} mmHg for 15 h, in order to remove physically adsorbed impurities. The surface area and the pore size distribution were determined by the BET and BJH methods, respectively. The BET specific surface area was calculated from the range P/P_0= 0.05–0.3 in the adsorption branch as well as the pore size distribution.

The reduction behaviour was studied by hydrogen temperature-programmed reduction (H_2-TPR) using a Micromeritics AutoChem II 2920 instrument with a thermal conductivity detector (TCD). The calcined and reduced samples were initially dried in an Ar stream at 150 ºC for 30 min (heating rate 10 ºC/min, total flow 50 mL/min) to ensure the complete elimination of possible traces of moisture. Then, a 10% H_2-Ar flow was passed through the bed containing the samples while the temperature was increased up to 950 ºC (heating rate 10 ºC/min, total flow 50 mL/min) and held for 30 min.

The calcined, reduced and used catalysts were also characterized by X-ray diffraction (XRD) in a RIGAKU D/max 2500 diffractometer. The instrument was equipped with Cu Kα radiation (λ = 0.15418 nm) and a graphite monochromator operated at atmospheric temperature and 40 kV as well as 80 mA. Each sample was scanned from

10º to 85º (2θ) at a rate of 0.03º/s. Phase identification was conducted by comparison with JCPDS data cards.

The acidity of the calcined catalysts was investigated by temperature-programmed desorption of ammonia (NH_3-TPD). The tests were performed again using a Micromeritics AutoChem II 2920 instrument with a thermal conductivity detector (TCD). The calcined samples were first dried in a He stream at 450 ºC for 1 h (heating rate 10 ºC/min, total flow 50 mL/min) and then cooled at 100 ºC. The ammonia adsorption was carried out at 100 ºC using a mixture of 0.5 % NH_3/He with a flow rate of 50 mL/min for 1 h. After the adsorption, the samples were purged with flowing He at 100 ºC for 1 h to remove the physisorbed ammonia. Desorption of the chemisorbed ammonia was measured by heating the samples up to 770 ºC at a rate of 10 ºC/min (total flow 30 mL/min).

The catalyst morphology was studied by field emission scanning electron microscopy (FESEM) using a Carl Zeiss MERLIN^{TM}, equipped with secondary and backscattered electron detectors in the chamber and column (in-lens). Moreover, the instrument was equipped with an EDS detector (INCA 350 from Oxford Instruments with energy resolution of 127 eV at 5.9 keV) for chemical analysis.

The scanning transmission electron microscopy (STEM) was applied to determine the size of the metallic crystallites. STEM analysis was carried out with a Tecnai F30 microscope (FEI Company) at a working voltage of 300 kV. High Angle Annular Dark Field (STEM-HAADF) images were obtained with a HAADF detector (Fischione). In this mode, the intensity of the signal is proportional to the square of the atomic number (Z^2), therefore heavier elements appear with a much brighter contrast than lighter elements. Also, in order to analyse the chemical composition of the material, X-ray

energy dispersive spectra (EDS) were obtained with an EDAX detector. First, the samples were dispersed in ethanol using an ultrasonic bath. Then, a droplet of suspension was added to a holey copper grid coated with a carbon film. Once the ethanol was evaporated into the atmosphere, the material was retained on the grid for analysis.

2.3 Catalyst performance

Catalytic performance was evaluated using a laboratory-scale continuous feeding unit designed and developed by PID (Process Integral Development Eng & Tech, Spain), described in previous works [5, 16]. The main characteristics of the installation are the stainless-steel tubular reactor (Autoclave Engineers) with an inner diameter of 9 mm and the micrometric valve, which regulates the system pressure. A PID control system (TOHO Digital Controller) keeps the reactor pressure stable during the experiments, while a display shows the live pressure values. A glycerol aqueous solution in deionized water is fed into the reactor by means of a high-performance liquid chromatography (HPLC) pump (Gilson model). A schematic diagram of the experimental system is shown in Fig. 1.

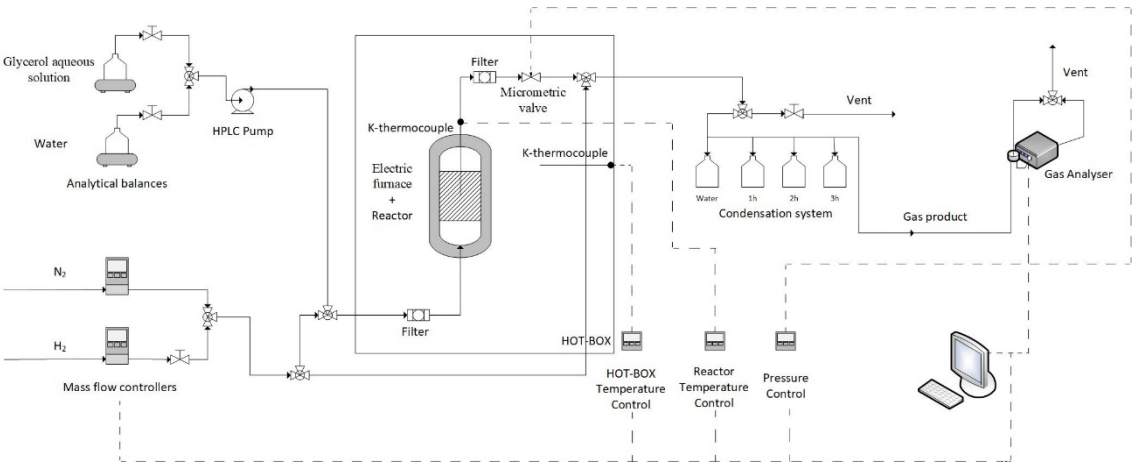

Fig. 1. Schematic diagram of the APH experimental rig.

The stream from the upper part of the reactor containing gas and liquid products and the unreacted glycerol passes through the micrometric valve. In this valve, the stream is depressurized and then goes to the condensation system. This system consists of four condensers. The first one was used to collect the water used to pressurize the system until reaching reaction conditions. In the other condensers, the liquid products were separated from the gas mixture and collected at intervals of 1 h during the experimental test until the total reaction time was complete (3 h).

The exit gas mixture was made up of N_2, used as an internal standard, and the different gaseous products of the APH reaction. This gas stream was analysed online with an Agilent 490 Micro-GC equipped with Thermal Conductivity Detectors (TCD), where N_2, H_2, CH_4, CO_2, CO, C_2H_6 and C_3H_8 were quantified. The N_2 flow was 75 cm^3 (STP)/min and was fed by means of a mass flow controller (Hi-Tec Bronkhorst).

The liquid fractions collected in the condensers were analysed offline with an Agilent 7820A GC. This was equipped with a Flame Ionization Detector (FID) and a HP-FFAP Agilent 19091F-105 capillary column, where methanol (MeOH), ethanol (EtOH), acetol, acetic acid, 1,2-propanediol (1,2-PDO), ethylene glycol (EG) and non-reacted glycerol were quantified. 1-butanol was used such as the internal standard. The injector and detector temperatures were 275 ºC and 300 ºC, respectively.

Catalytic tests were performed under the same operating conditions for all the catalysts in order to study the effect of the molar ratio of Al/Fe on the Ni catalyst. Each experiment lasted 3 h at 227 ºC and 34 absolute bar. A solution of 10 wt.% glycerol (Sigma-Aldrich, purity: ≥ 99.5 %) in distilled water was used as feed (total flow 1 mL/min) and a mass of catalyst/ glycerol mass flow rate ratio (W/m) of 20 $g_{catalyst} \cdot min/g_{glycerol}$. The weight of the fixed bed was 7 g, with 2 g of catalyst and the rest

inert sand with the same mesh size as the catalyst (160 - 315 μm). The experiments were performed twice to check their repeatability, obtaining a standard deviation below 3 % of the following variables: glycerol conversion, carbon yield to gases, carbon yield to liquids and carbon selectivity to liquids.

Prior to the start of each experiment, the calcined catalyst with Fe (Ni/Al_3Fe_1, Ni/Al_1Fe_1, Ni/Al_1Fe_3 and Ni/Fe) and the calcined catalyst without Fe (Ni/Al) were reduced in situ at 500 ºC and 600 ºC during 1 h, respectively, using a H_2 stream of 100 cm^3 (STP)/min. The reduction temperature was selected according to the H_2-TPR results. The catalytic performance was calculated according to expressions (1) - (6) below.

The global glycerol conversion was calculated as follows:

$$Glycerol\ conversion\ (\%) = \frac{n^{in}_{glycerol} - n^{out}_{glycerol}}{n^{in}_{glycerol}}\ x\ 100 \quad (1)$$

where $n^{in}_{glycerol}$ and $n^{out}_{glycerol}$ are the moles of glycerol fed and the moles of unreacted glycerol in the exit liquid, respectively. These $n^{in}_{glycerol}$ and $n^{out}_{glycerol}$ are the values for the whole experiment (3 h).

The hydrogen and alkane yields were defined as follows:

$$H_2\ yield\ (\%) = \frac{n_{H_2}}{n^{in}_{glycerol}\ x\ 7}\ x\ 100 \quad (2)$$

$$Alkane\ yield\ (\%) = \frac{n_{CH_4} + 2n_{C_2H_6} + 3n_{C_3H_8}}{n^{in}_{glycerol}\ x\ 3} x\ 100 \quad (3)$$

The carbon yield to gases and carbon yield to liquid were defined as follows:

$$Carbon\ yield\ to\ gases\ (\%) = \frac{n_{CO} + n_{CO_2} + n_{CH_4} + 2n_{C_2H_6} + 3n_{C_3H_8}}{3\ x\ n^{in}_{glycerol}}\ x\ 100 \quad (4)$$

$$Carbon\ yield\ to\ liquid\ (\%) = \frac{n_{MeOH} + 2n_{EtOH} + 2n_{Acetic\ acid} + 3n_{Acetol} + 3n_{1,2-PDO} + 2n_{EG}}{3\ x\ n^{in}_{glycerol}}\ x\ 100 \qquad (5)$$

where n_i are the moles of the i product (i = liquid and gas products)

There is a slight difference between the glycerol conversion and the addition of the carbon yield to products (gases and liquids). This could be due to errors in collecting and analysing the samples and, most important, to unidentified compounds in the collected liquids. A carbon deficit smaller than 15 % was considered acceptable for the experiment reliability, as proposed by other authors [16, 19]. The carbon deficit was defined as follows:

$$Carbon\ deficit = Glycerol\ conversion - (carbon\ yield\ to\ gases + carbon\ yield\ to\ liquids) \qquad (6)$$

The liquid carbon selectivity was defined as the percentage ratio of carbon in a liquid product to the total carbon in all the liquid products analysed. Glycerol was not considered.

The gas compositions were determined in N_2 and H_2O free basis.

3. Results and discussion

3.1 Catalytic performance in the APH of glycerol

Fig. 2 shows the carbon yield to gases, carbon yield to liquids and glycerol conversion obtained in the activity tests performed at 227 ºC and 34 absolute bar for different catalysts. The Ni/Al_3Fe_1 catalyst presents the highest glycerol conversion (42.31%), carbon yield to gases (6.57%) and carbon yield to liquids (30.45%). The carbon yield to liquids is higher than to gases for all the catalysts studied because at these operation conditions liquid production is more favoured than gas production [16].

For the Ni/Al_3Fe_1 catalyst, which shows the highest measured rate of reaction, Weisz-Prater and Mears' criteria have been calculated to determine if internal diffusion and external mass transfer can be neglected, respectively. The values of these criteria confirm the kinetic regime under the experimental conditions tested. There are two different trends. Firstly, when Fe is added to the Ni/Al catalyst, there is an increase in the glycerol conversion (from 24.73% to 42.31%), carbon yield to gases (from 5.07% to 6.57%) and carbon yield to liquids (from 16.67% to 30.45%) from Ni/Al to Ni/Al_3Fe_1. Secondly, as the Fe content of the catalyst increases, a change in trend is observed since the glycerol conversion, carbon yield to gases as well as the carbon yield to liquid decrease from 42.31% to 2.94%, 6.57% to 0.02% and 30.45% to 0.76%, respectively, with the increasing of Fe in the catalyst, from Ni/Al_3Fe_1 to Ni/Fe. Hence, it is observed that the mixed oxide supports present higher catalytic activity than Ni/Al and Ni/Fe catalysts. Bastan et al. [28] reported the same tendency with the Ni/Al_2O_3-MgO catalysts. Finally, it is concluded that the catalytic activity decreases in the following order: $Ni/Al_3Fe_1 > Ni/Al_1Fe_1 > Ni/Al_1Fe_3 > Ni/Al > Ni/Fe$.

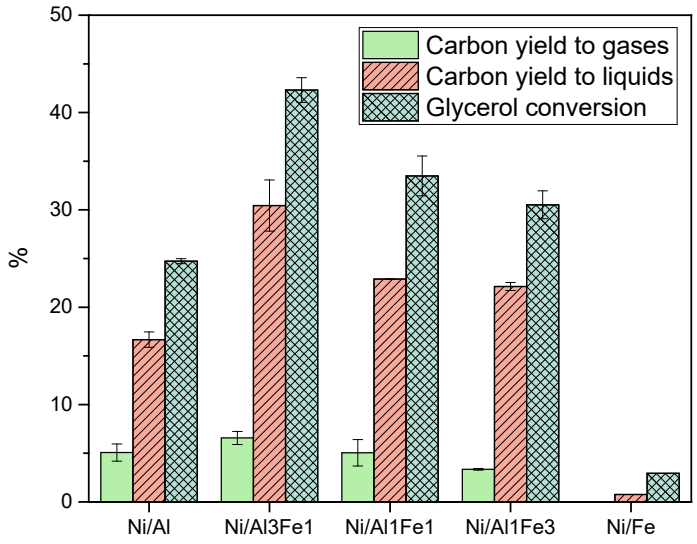

Fig. 2. Glycerol conversion and carbon yield to gases and liquids for different catalysts.

Table 1 shows the results corresponding to the gases stream, including the gas compositions (vol.%, N_2 and H_2O free), hydrogen and alkane yields. For all the catalysts, the main gases are H_2 and CO_2 and low amounts of CH_4, C_2H_6, C_3H_8 and CO are obtained in the exit gas. The H_2 and alkane yields follow the same tendency as the carbon yield to gas, Ni/Al_3Fe_1 being the catalyst with the highest values of H_2 yield (0.45%) and alkane yield (1.10%). Moreover, it is observed that the alkane yield is higher than the H_2 yield for all the catalysts, except for the Ni/Fe catalyst. It is possible that the C-O scission, which occurs in the acid sites, leads to alkane production [31]. In addition, the alkane/H_2 yield ratio decreases from 2.66 to zero with the increase in the Fe content.

Table 1. Gas compositions (vol.%, N_2 and H_2O free), hydrogen and alkane yields.

Catalyst	Ni/Al	Ni/Al_3Fe_1	Ni/Al_1Fe_1	Ni/Al_1Fe_3	Ni/Fe
Gas composition (vol.%, N_2 and H_2O free)					
H_2	16.63 ± 0.9	15.78 ± 1	12.69 ± 0.4	18.73 ± 1	93.8
CO_2	68.65 ± 7	70.62 ± 4	84.25 ± 0.5	77.11 ± 1	6.1
CO	0.10 ± 0.03	0.12 ± 0.06	0.00 ± 0.0	0.17 ± 0.1	0.0
CH_4	12.16 ± 7	11.12 ± 2	0.00 ± 0.0	0.00 ± 0.0	0.0
C_2H_6	1.70 ± 0.4	1.61 ± 0.1	2.24 ± 0.06	3.18 ± 0.06	0.0
C_3H_8	0.76 ± 0.09	0.76 ± 0.0	0.81 ± 0.01	0.81 ± 0.01	0.05
Gas yields (%)					
H_2	0.38 ± 0.09	0.45 ± 0.1	0.27 ± 0.06	0.28 ± 0.02	0.1
Alkane	1.01 ± 0.5	1.10 ± 0.3	0.34 ± 0.08	0.30 ± 0.0	0.0

The reaction network of the APH of glycerol includes gas and liquid products. There are two main routes in the liquid phase. Route 1 is the dehydration of glycerol to acetol and further hydrogenation to form 1,2-propanediol. This is the main route in glycerol hydrogenolysis. Route 2 is the dehydrogenation of glycerol, forming glyceraldehyde whose further decarbonylation generates ethylene glycol. Ethanol can produce acetic acid, while this alcohol can be generated from ethylene glycol by dehydration/hydrogenation. In addition, methanol can be produced from ethylene glycol by dehydrogenation/decarbonylation [16, 19].

Fig. 3 shows the global carbon selectivity to liquids. The liquid product with the highest carbon selectivity is 1,2-propanediol with the highest value around 70.89% for the Ni/Al_3Fe_1 catalyst. According to these results, under these experimental conditions route 1 is favoured with the production of 1,2-propanodiol from acetol. In addition, according to the literature [12, 13, 36] the dehydration of glycerol to acetol takes place in acid sites, and then the hydrogenation of acetol to 1,2-propanodiol occurs on the metal active sites of the catalyst. Thus, among other factors, the acidity of the support is important. Glyceraldehyde, an intermediate product in route 2, has not been detected in the analysis. However, route 2 is followed because of the existence of ethylene glycol that is obtained from the fast reaction of the decarbonylation of glyceraldehyde [21, 31]. Nevertheless, 95.36% of the acetol is obtained with the Ni/Fe catalyst because this catalyst probably will not produce the hydrogenation of acetol to 1,2-propanediol.

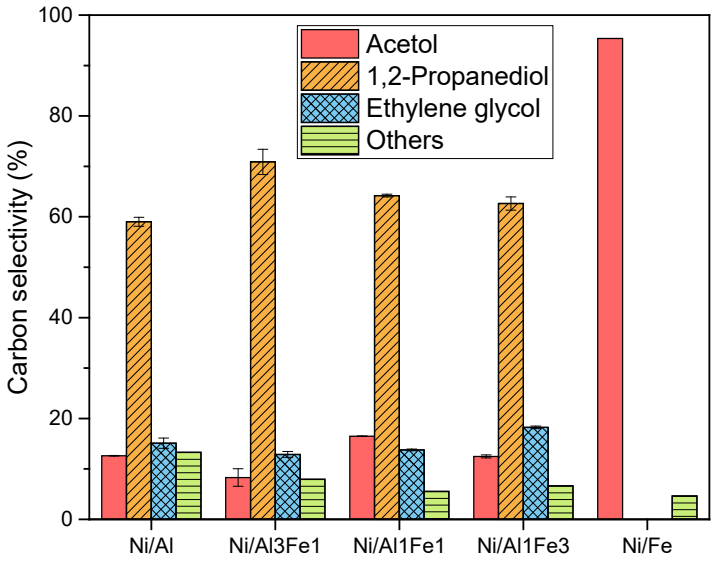

Fig. 3. Carbon selectivity to liquids of the different catalysts. Others: methanol, ethanol and acetic acid.

Table 2 shows a comparison between our results with the best catalyst (Ni/Al_3Fe_1) and other works in the literature that also studied the production of value-added products such as 1,2-propanediol, acetol and ethylene glycol from glycerol conversion. It may be deduced that the optimum value of the 1,2-propanediol (1,2-PDO) yield is 0.810 $g/g_{glycerol}$ which is obtained by glycerol hydrogenolysis with external H_2 feeding and employing a very high value of the $W/m_{glycerol}$ ratio [8]. It is observed that our catalyst presents the lowest value of glycerol conversion ($X_{glycerol}$) but approximately the same or greater value of the 1,2-PDO yield as other reports [16, 19, 27, 34]. This means that our catalyst is selective to this value-added product.

Table 2. Comparison with other works in the literature that also studied the production of value-added products such as 1,2-propanediol, acetol and ethylene glycol from glycerol conversion.

Catalyst	Operating conditions	Results	H_2 as feed	Reference
28Ni/Al[a]	227 ºC, 34 bar, 10 wt.% glycerol (W/m) = 20 $g_{catalyst}$·min/$g_{glycerol}$	$X_{glycerol}$ = 65.2%, 1,2-PDO yield = 0.169 g/$g_{glycerol}$ Acetol yield = 0.043 g/$g_{glycerol}$, EG yield* = 0.060 g/$g_{glycerol}$	Without H_2	García et al. [16]
CuNi/Al_2O_3[a]	250 ºC, 40 bar, 10 wt.% glycerol (W/m)* = 30 $g_{catalyst}$·min/$g_{glycerol}$	$X_{glycerol}$ = 82%, 1,2-PDO yield* = 0.198 g/$g_{glycerol}$ Acetol yield* = 0.105 g/$g_{glycerol}$	Without H_2	Freitas et al. [34]
CuNi/ZSM-5[a]	250 ºC, 40 bar, 10 wt.% glycerol (W/m)* = 30 $g_{catalyst}$·min/$g_{glycerol}$	$X_{glycerol}$ = 87%, 1,2-PDO yield* = 0.223 g/$g_{glycerol}$ Acetol yield* = 0.040 g/$g_{glycerol}$	Without H_2	Freitas et al. [34]
3CuB/SiO_2[a]	200 ºC, 50 bar, 10 wt.% glycerol (W/m)* = 800 $g_{catalyst}$·min/$g_{glycerol}$	$X_{glycerol}$ = 100%, 1,2-PDO yield* = 0.810 g/$g_{glycerol}$ Acetol yield* = 0.004 g/$g_{glycerol}$, EG yield* = 0.003 g/$g_{glycerol}$	With H_2	Zhu et al. [8]
5Ru/Al_2O_3 + 5Pt/Al_2O_3[b]	220 ºC, 14 bar, 10 wt.% glycerol (W/W)* = 0.083 $g_{catalyst}$·min/$g_{glycerol}$	$X_{glycerol}$ = 50.2%, 1,2-PDO yield* = 0.196 g/$g_{glycerol}$ EG yield* = 0.032 g/$g_{glycerol}$	Without H_2	Roy et al. [19]
65Ni/SiO_2-Al_2O_3[b]	240 ºC, autogenous pressure, 10 wt.% glycerol (W/W)* = 0.25 $g_{catalyst}$·min/$g_{glycerol}$	$X_{glycerol}$ = 76%, 1,2-PDO yield* = 0.065 g/$g_{glycerol}$ Acetol yield* = 0.012 g/$g_{glycerol}$, EG yield* = 0.016 g/$g_{glycerol}$	Without H_2	Seretis and Tsiakaras [27]
Ni/Cu/γ-Al_2O_3[a]	230 ºC, 35 bar, 10 wt.% glycerol (W/m)* = 155 $g_{catalyst}$·min/$g_{glycerol}$	$X_{glycerol}$ = 77.9%, 1,2-PDO yield* = 0.422 g/$g_{glycerol}$ Acetol yield* = 0.086 g/$g_{glycerol}$	2-propanol (H_2 source)	Cai et al. [13]
Ni/Cu/TiO_2[a]	230 ºC, 35 bar, 10 wt.% glycerol (W/m)* = 155 $g_{catalyst}$·min/$g_{glycerol}$	$X_{glycerol}$ = 84.6%, 1,2-PDO yield* = 0.518 g/$g_{glycerol}$ Acetol yield* = 0.076 g/$g_{glycerol}$	2-propanol (H_2 source)	Cai et al. [13]
28Ni/Al_3Fe_1[a]	227 ºC, 34 bar, 10 wt.% glycerol (W/m) = 20 $g_{catalyst}$·min/$g_{glycerol}$	$X_{glycerol}$ = 42.3%, 1,2-PDO yield = 0.178 g/$g_{glycerol}$ Acetol yield = 0.021 g/$g_{glycerol}$, EG yield = 0.040 g/$g_{glycerol}$	Without H_2	Present work

a: Fixed bed reactor, b: Batch reactor, *: Estimated values are calculated from data provided in the reference, W/m: mass of catalyst/ glycerol mass flow rate ratio ($g_{catalyst}$·min/$g_{glycerol}$), W/W: mass of catalyst/ mass of glycerol ratio ($g_{catalyst}$/$g_{glycerol}$)

3.2 Catalyst characterization

Table 3 shows the results of the ICP-OES. For all the catalysts, the synthesis is appropriate except for the Ni/Fe. There is a difference between the analysis and theoretical results for the Ni/Fe catalyst because during the synthesis it is difficult to precipitate the Ni. This means that more Fe is precipitated than Ni. Moreover, Fe precipitates at a lower pH than Ni [39].

Table 3. Metal content in the catalysts expressed as molar % determined by ICP-OES.

	Theoretical (molar%)			Analysis (molar %)		
	Fe	Al	Ni	Fe	Al	Ni
Ni/Al	-	72	28	-	71.7	28.3
Ni/Al_3Fe_1	18	54	28	18.0	54.2	27.8
Ni/Al_1Fe_1	36	36	28	34.7	38.1	27.2
Ni/Al_1Fe_3	54	18	28	53.0	19.6	27.3
Ni/Fe	72	-	28	80.9	-	19.1

According to the IUPAC classification [40], the N_2 adsorption-desorption isotherms of the calcined and used catalysts shown in Fig.4 (A) and (B), respectively, correspond to the type IV isotherm. A hysteresis loop occurred after $p/p_o = 0.4$ in the adsorption-desorption isotherm of the catalysts, characteristic of mesoporous materials. It is well known that Al_2O_3 is a mesoporous material and its presence in the catalysts except the Ni/Fe catalyst favours the mesoporous structure. However, the Ni/Fe catalyst also presents a type IV isotherm, and it is possible that Fe oxides could provide the mesoporous structure. Different hysteresis loops are found for the calcined catalysts compared with some of the used catalysts. The calcined catalysts and two of the used

catalysts (Ni/Al and Ni/Al_3Fe_1) present a hysteresis loop of type H2 characteristic of a mesoporous solid with interconnected pores of different size and shape. Conversely, the other used catalysts (Ni/Al_1Fe_1, Ni/Al_1Fe_3 and Ni/Fe) present hysteresis loops of type H3 associated with non-rigid aggregates of plate-like particles [40, 41].

The textural properties of all the samples are depicted in Table 4, while the corresponding surface areas of the calcined and used catalysts are shown in Fig. 4 (C). For the calcined catalysts, the introduction of Fe produces a decrease in the surface area (S_{BET}) but an increase in the average pore diameter (d_p). However, the pore volume presents a maximum with the Ni/Al_3Fe_1 catalyst, which is the most active. A clear decrease in the surface area is observed after using the catalysts. In addition, the catalyst that least reduced is Ni/Al_3Fe_1. Besides, it is observed that the Ni/Fe catalyst presented the highest decrease in the surface area and the worst catalytic performance results.

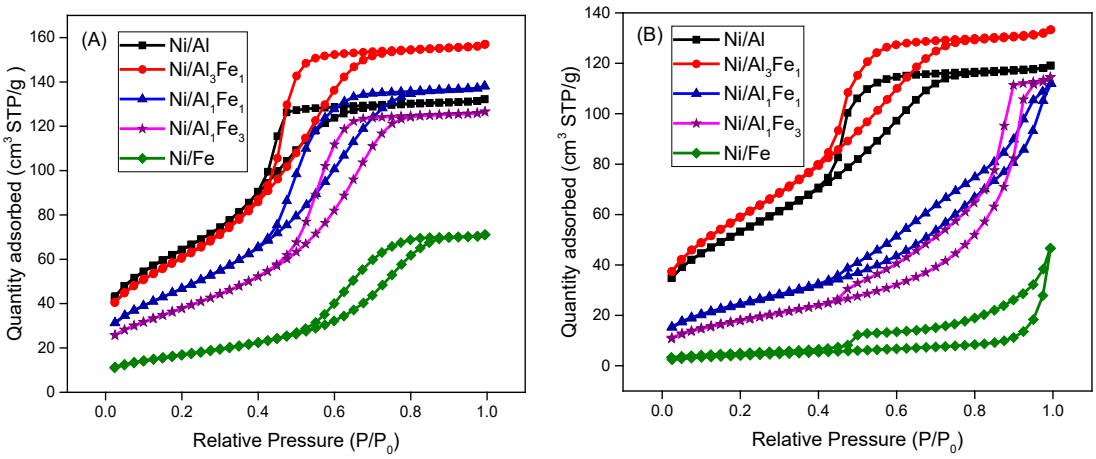

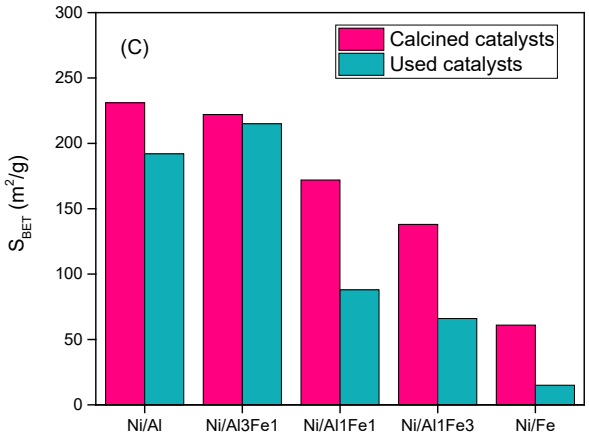

Fig. 4. N_2 adsorption-desorption isotherms of the calcined (A) and used (B) catalysts. Surface area of the catalysts (C).

Table 4. Textural properties of the catalysts and boehmite crystallite size.

Composition		Calcined catalysts			Used catalysts			XRD
	(molar ratio of Al/Fe)	S_{BET}[a] (m^2/g)	V_p[b] (cm^3/g)	d_p[b] (nm)	S_{BET}[a] (m^2/g)	V_p[b] (cm^3/g)	d_p[b] (nm)	D[c] (nm)
Ni/Al	1/0	231	0.144	3.31	192	0.130	4.18	5.1
Ni/Al_3Fe_1	3/1	222	0.211	3.93	215	0.151	3.94	6.2
Ni/Al_1Fe_1	1/1	172	0.193	4.45	88	0.158	5.39	6.6
Ni/Al_1Fe_3	1/3	138	0.184	5.81	66	0.168	9.00	-
Ni/Fe	0/1	61	0.106	7.41	15	0.040	3.14	-

a: BET method.

b: BJH adsorption method.

c: Boehmite crystal size calculated from Scherrer equation.

The XRD patterns of the calcined catalysts are presented in Fig. 5 (A). All the catalysts are quite amorphous except the Ni/Fe catalyst. The wide diffraction peaks and the low intensities make it difficult to assign the phases. However, some phases can be

elucidated. The phases identified in the Ni/Al catalyst are NiO (bunsenite, JCPDS 00-001-1239) and γ-Al_2O_3 (JCPDS 00-029-0063). Also, the diffraction peaks of $NiAl_2O_4$ are seen at 2θ of 37.0º, 45.0º and 65.5º (JCPDS 00-010-0339). According to Alzamora et al. [42], at low calcination temperatures, the calcined hydrotalcites consist of two different phases: 1) a crystalline NiO phase that contains Al^{3+} ion and 2) a γ-Al_2O_3 structure which might contain Ni^{2+} ions. The $NiAl_2O_4$ phase is obtained by the interaction between NiO and Al_2O_3 during the calcination and its presence depends on the Ni/Al molar ratio and the calcination temperature [42]. The diffraction peaks of $NiAl_2O_4$ and γ-Al_2O_3 are observed in the Ni/Al_3Fe_1 catalyst. Meanwhile, these diffraction peaks are missing from the Ni/Al_1Fe_1 and Ni/Al_1Fe_3 catalysts which contain less Al. It is clear that the presence of the $NiAl_2O_4$ phase diminishes with the increase in the Fe content and the decrease in the Al content, as reported by Meng et al. [38]. With the addition of Fe, the Fe_2O_3 (JCPDS 00-001-1053) and Fe_3O_4 (JCPDS 00-001-1111) phases are identified and their content rises with the increase in the Fe content. The $NiFe_2O_4$ phase (JCPDS 01-086-2267) is identified in the Ni/Al_1Fe_1 and Ni/Al_1Fe_3 catalysts, which is formed during the calcination due to the interaction between NiO and Fe_2O_3 [37]. Furthermore, $FeAl_2O_4$ (JCPDS 01-086-2320) is observed in the mixed oxide supports (Ni/Al_3Fe_1, Ni/Al_1Fe_1 and Ni/Al_1Fe_3 catalysts). The phases identified in the Ni/Fe catalyst are NiO, Fe_2O_3 and Fe_3O_4.

Conversely, Fig. 5 (B) and (C) show the XRD patterns of the reduced and used catalysts, respectively. The phases present in the spent catalysts are very similar to the reduced catalysts, except the boehmite phase. The structure of the calcined catalysts changed after the reaction and their prior reduction, becoming more crystalline. The characteristic peaks of the Ni phase at 2θ of 44.5º, 51.8º and 76.4º (JCPDS 01-087-0712) are observed in the Ni/Al catalyst. The boehmite phase (AlOOH) appears with

the main reflections at 14.4º, 28.1º, 38.3º, 48.9º and 71.9º (JCPDS 01-074-1895) in the Ni/Al catalyst, as reported by Freitas et al. [34], as well as in the Ni/Al_3Fe_1 and Ni/Al_1Fe_1 catalysts. The boehmite phase is formed from the reaction of Al_2O_3 with H_2O. According to Freitas et al. [34], the presence of metal particles retards the formation of boehmite from the γ-alumina, and our results corroborate this effect. The reduction in the main boehmite peak at 2θ = 14.4 º indicates that the boehmite content decreases with an increase in the Fe content in the catalyst. Besides, the boehmite crystallite size increases from 5 to 7 nm with the increase in the Fe content (Table 4). The average boehmite crystallite sizes are calculated using the Scherrer equation for the boehmite diffraction peak at 2θ = 14.4 º [43, 44]. The SiO_2 crystalline phase (JCPDS 00-046-1045) was observed in the Ni/Al, Ni/Al_1Fe_3 and Ni/Fe used catalysts. The APH of glycerol reaction takes place in a fixed bed reactor with a mix of catalyst and sand. Therefore, the presence of SiO_2 in the catalysts is a result of the incomplete separation of the catalyst from the sand before the characterization. In addition, the diffraction peaks of $FeNi_3$ phase at 2θ of 44.1º, 51.4º and 75.7º (JCPDS 03-065-3244) and $AlNi_3$ phase at 2θ of 43.6º, 50.7º and 75.0º (JCPDS 00-050-1265) could be observed in the Ni/Al_3Fe_1, Ni/Al_1Fe_1 and Ni/Al_1Fe_3 catalysts. The presence of $FeNi_3$ phase in the catalysts with mixed oxide supports could favour the hydrogenation of acetol to 1,2-propanediol and the glycerol conversion (Fig. 1) according to the results obtained, where the Ni/Al_3Fe_1 catalyst showed the maximum glycerol conversion (42.31%), carbon yield to gases (6.57 %) and carbon yield to liquids (30.45%).These three catalysts (Ni/Al_3Fe_1, Ni/Al_1Fe_1 and Ni/Al_1Fe_3) show high carbon selectivity to 1,2-propanediol.

The review by Shi et al. [45] explained the benefits of the Ni-Fe nanoparticles in comparison with the Ni monometallic system for the catalytic hydrogenation of organic

molecules. Ni-Fe nanoparticles present higher rates and selectivity than Ni monometallic for the hydrogenation of C=C, C=O and C=N bonds. For instance, the $Ni_{75}Fe_{25}$ formulation favours CO and CO_2 hydrogenation, while the $Ni_{80}Fe_{20}$ formulation is the most active for dry and steam reforming among other formulations [45]. Li et al. [46] found that the formation of $FeNi_3$ during the reduction was beneficial for the dry reforming of methane (DRM) reaction. They concluded that the presence of $FeNi_3$ favoured the DRM reaction because the FeNiAl catalyst had better catalytic behaviour than the NiAl catalyst [46]. Meng et al. [38] reported that the formation of the Ni-Fe alloy during the reduction was an important factor for the CO methanation reaction over the Ni species that existed in the catalyst.

The Fe_3O_4 phase is still observed in the catalysts that contain Fe but its presence in the Ni/Fe catalyst could be minimal due to its total reducibility after the reduction treatment. Moreover, the Fe_2O_3 phase is missing from these catalysts. The diffraction peaks of $FeAl_2O_4$ are still detected in the mixed oxide supports. In addition, the $NiFe_2O_4$ phase is still observed in the Ni/Al_1Fe_1 and Ni/Al_1Fe_3 catalysts. The patterns of the Fe_3O_4, $FeAl_2O_4$ and $NiFe_2O_4$ are similar, especially the main intensity peak at 2θ of around 36º, thus these phases could be present in the above-mentioned catalysts.

The diffraction peaks at 43.5º, 50.7º and 74.7º and at 44.6º, 65.0º and 82.3º are attributed to taenite (JCPDS 00-047-1417) and kamacite (JCPDS 03-065-7752), respectively, which are detected in the Ni/Fe catalyst. The Ni-Fe alloys (taenite and kamacite) do not favour the APH of glycerol.

The Ni, $FeNi_3$ and kamacite average crystallite sizes were calculated using the Scherrer equation for the diffraction peak at 2θ = 44.5 º, 44.1 º and 44.6 º, respectively [43, 44]. For the Ni/Al_3Fe_1, Ni/Al_1Fe_1 and Ni/Al_1Fe_3 catalysts, the diffraction peaks of $FeNi_3$ and

$AlNi_3$ phases are very close and both phases could be found. The Ni/Al_3Fe_1 catalyst had the smallest crystallite size, and this was the catalyst with highest activity. Although the Ni/Al catalyst had a smaller crystallite than the other two catalysts with mixed oxide supports, these catalysts had a higher activity than the Ni/Al catalyst. This could be because the $FeNi_3$ phase has an important role in the aqueous phase hydrogenolysis of glycerol (Table 5 (A)). During 3 h of the reaction, deactivation of the catalysts was not appreciated. This means that the catalytic activity is due to the phases present in the reduced catalysts, mainly the Ni metal for the Ni/Al catalyst and $FeNi_3$ for the catalysts with mixed oxide supports. The reaction time was too short to study the catalyst stability.

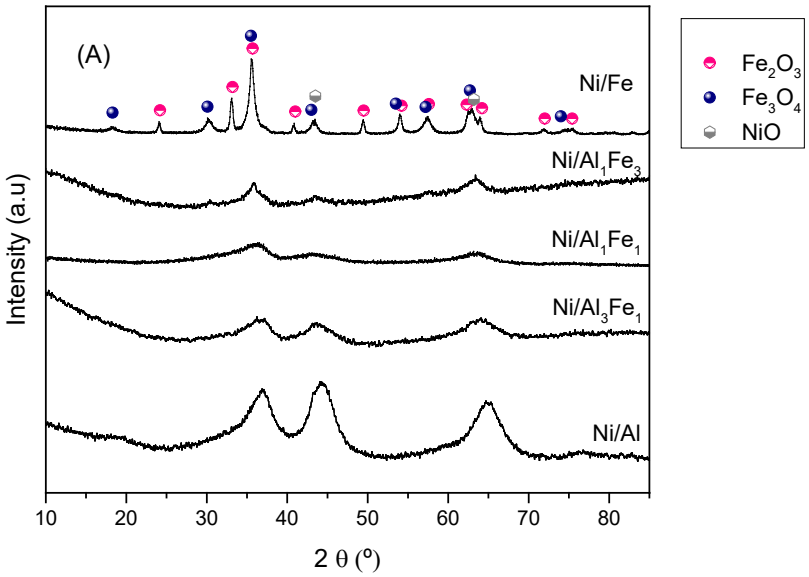

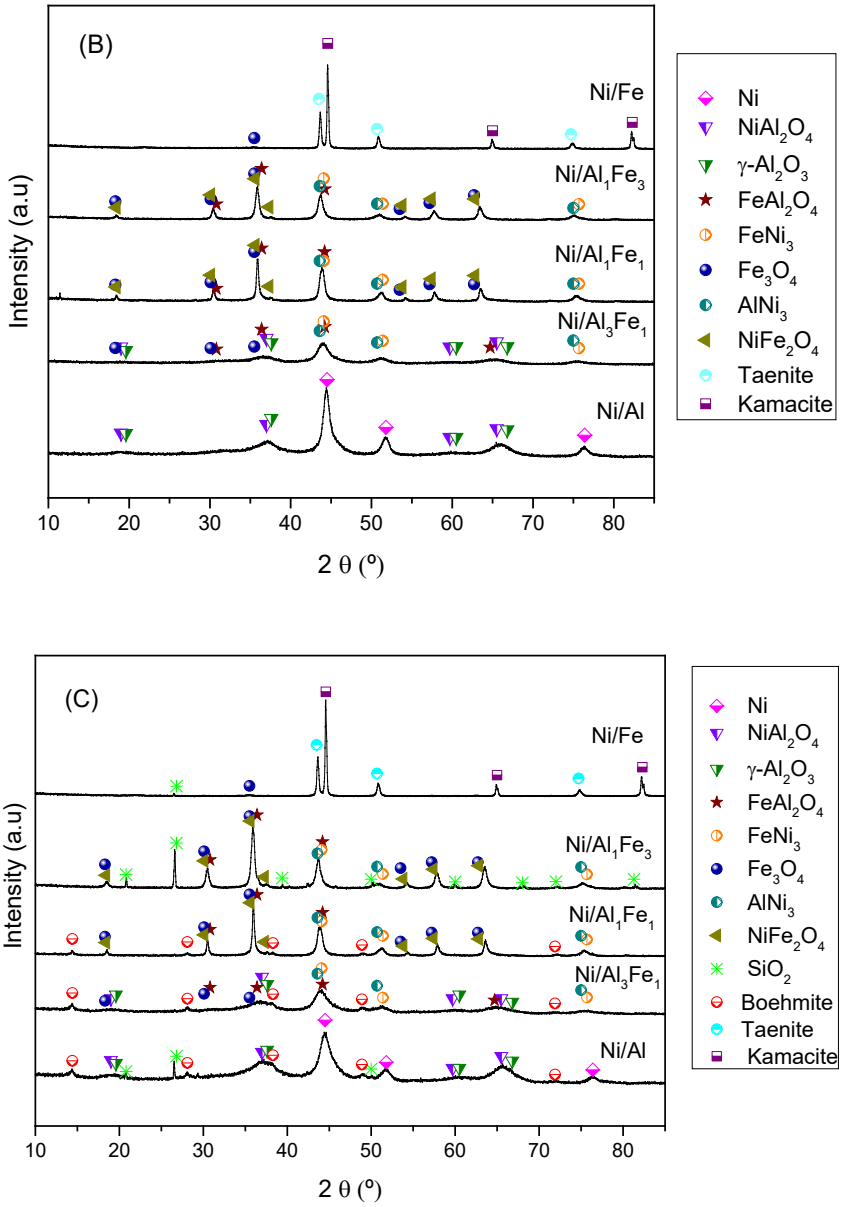

Fig. 5. XRD patterns of the calcined (A), reduced (B) and used (C) catalysts.

The H_2-TPR profiles of the calcined and reduced catalysts are shown in Fig. 6 (A) and (B), respectively. Peaks were observed in the reduced catalysts below 600 ºC for the Ni/Al catalyst and 500 ºC for the rest. This could be due to the reoxidation of the catalysts during their previous handling at room temperature. In order to clarify the reduction of the phases present in the catalysts, Gaussian-fitting analysis was conducted. Tables 5 (A) and (B) present the results of this analysis and the assignation of phases for the calcined and reduced catalysts, respectively. The assignation of phases was carried

out considering the results of the XRD characterization and references from the literature [38, 47, 48]. The α–type NiO species correspond to NiO phase with weak interaction with the support, while the γ-type NiO species are attributed to the reduction of $NiAl_2O_4$ phase or Ni phases with strong interaction with the support. The peaks at high temperatures are attributed to the reduction of $FeAl_2O_4$, $NiFe_2O_4$ and $NiAl_2O_4$ phases. For the Ni/Al_1Fe_1 and Ni/Al_1Fe_3 calcined catalysts, the wide curves centred at 665 and 735 ºC, respectively, could be attributed to the reduction of $FeAl_2O_4$ and $NiFe_2O_4$.

In general, the peaks in the low temperature range of 200 - 440 ºC are attributed to the reduction of the α-type NiO species and the reduction peak of Fe_2O_3 to Fe_3O_4. The peak in the medium temperature range of 440 - 600 ºC is ascribed to the reduction peak of Fe_3O_4 to Fe. Moreover, the peak in the temperature range of 550 - 750 ºC is assigned to the reduction of the γ-type NiO species [38].

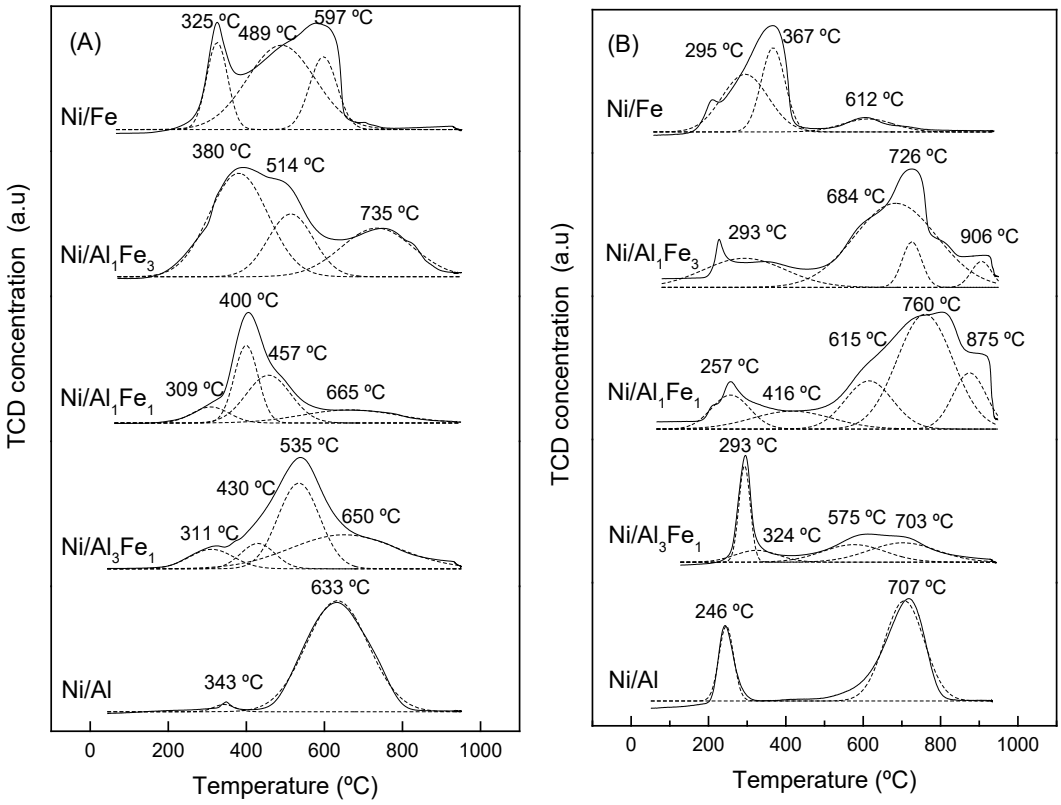

Fig. 6. H_2-TPR profiles of the calcined (A) and reduced (B) catalysts

The total reduction of phases that include Ni and Fe during the reduction treatment has been estimated. The total H_2 consumption of the calcined catalyst and the H_2 consumption at temperatures higher than the reduction treatment in the reduced catalyst were calculated. The results show around 60% of total reduction for the Ni/Al, Ni/Al_3Fe_1 and Ni/Al_1Fe_1 catalysts, 45 % for the Ni/Al_1Fe_3 catalyst and 99% for the Ni/Fe catalyst.

The unreduced phases after the reduction treatment are the γ-type NiO species in the Ni/Al catalyst and Fe_3O_4, $NiAl_2O_4$, $FeAl_2O_4$ and $NiFe_2O_4$ in the catalysts with mixed oxide supports. This could indicate that a high proportion of Ni has been reduced. Meng et al. [38] have suggested that the increase in the Fe content improves the reduction of NiO species in Ni/Al-Fe catalysts. The Ni/Fe catalyst shows that almost the totality of the Ni and Fe phases were reduced.

Under the reaction conditions, the catalysts with mixed oxide supports, Ni/Al_3Fe_1, Ni/Al_1Fe_1 and Ni/Al_1Fe_3, may show a high proportion of reduced Ni phases and the formation of Ni-Fe alloys, such as $FeNi_3$. This has a positive influence on the catalytic performance, with high glycerol conversion and high selectivity to 1,2-propanediol.

Table 5 (A). Gaussian fitting analysis of H_2-TPR patterns of the calcined catalysts and Ni, $FeNi_3$ and kamacite crystalline sizes of the used catalysts.

Total H_2 consumption		Reduction temperature (ºC)/Relative content (%)						XRD[a]
	(mmol/g)	α-NiO	Fe_2O_3	Fe_3O_4	$NiFe_2O_4$	$FeAl_2O_4$	γ-NiO	(nm)
Ni/Al	4.90	343/2.1	-	-	-	-	633/97.9	4.5
Ni/Al_3Fe_1	8.28	311/5.6	430/9.9	535/36.6	-	650/47.9[*]		3.8
Ni/Al_1Fe_1	15.13	309/8.4	400/30.5	457/36.4	665/19.9[**]		-	11.8
Ni/Al_1Fe_3	16.94	380/38.7[***]		514/36.0	735/25.3		-	12.5
Ni/Fe	23.44	325/18.5	489/60.3	597/21.2	-	-	-	39.9

[*]: Value corresponding to total reduction of $NiAl_2O_4$ and $FeAl_2O_4$.

[**]: Value corresponding to total reduction of $NiFe_2O_4$. and $FeAl_2O_4$.

[***]: Value corresponding to total reduction of α-NiO and Fe_2O_3.

[a]: Ni (Ni/Al), $FeNi_3$ (Ni/Al_3Fe_1, Ni/Al_1Fe_1 and Ni/Al_1Fe_3) and kamacite (Ni/Fe) crystal sizes calculated from Scherrer equation.

Table 5 (B). Gaussian fitting analysis of H_2-TPR patterns of the reduced catalysts.

Total H_2 consumption ($mmol/g_{catalyst}$)	Reduction temperature (ºC)/Relative content (%)					
	α-NiO	Fe_2O_3	Fe_3O_4	γ-NiO	$FeAl_2O_4$	$NiFe_2O_4$
Ni/Al 2.50	246/21.1	-	-	707/78.9	-	-
Ni/Al_3Fe_1 5.38	293/26.6	324/11.7	575/32.0	703/29.8*		-
Ni/Al_1Fe_1 7.83	257/7.4	416/17.2	615/32.7	-	760/26.4	875/16.3
Ni/Al_1Fe_3 11.05	293/15.2**		684/55.8	-	726/13.3	906/15.7
Ni/Fe 1.60	295/49.1	367/38.2	612/12.7	-	-	-

*: Value corresponding to total reduction of $NiAl_2O_4$ and $FeAl_2O_4$.

**: Value corresponding to total reduction of α-NiO and Fe_2O_3.

NH_3-TPD was carried out to determine the acidity of the catalyst. In order to demonstrate the kinds of desorption regions, Gaussian-fitting analysis was conducted (Table 6 and Fig. 7). For the Ni/Al and Ni/Al_3Fe_1 catalysts, there are three main regions. For the Ni/Al_1Fe_1 and Ni/Al_1Fe_3 catalysts, there are four. Finally, five different regions can be observed for the Ni/Fe catalyst. The strength of the acid sites can be classified as weak (< 200 ºC, T1), low moderate (200-300 ºC, T2), moderate (300-450 ºC, T3), strong (450-700 ºC, T4) and very strong (> 700 ºC, T5). According to previous reports [13, 25], the acid sites of catalysts include weak acid (< 200 ºC), moderate (200 – 450 ºC) and strong (450 – 750 ºC).

Table 6. NH_3-TPD results of the calcined catalysts and TEM results of the used catalysts.

	Temperature (ºC)					Strength (%)[a]					μmol $NH_3/g_{catalyst}$	STEM[b]
	T1	T2	T3	T4	T5	F1	F2	F3	F4	F5		(nm)
Ni/Al	187	286	-	593	-	11	36	-	53	-	891.65	12.3
Ni/Al_3Fe_1	175	269	-	588	-	7	50	-	43	-	820.22	8.4
Ni/Al_1Fe_1	170	257	-	571	754	7	60	-	31	2	459.58	-
Ni/Al_1Fe_3	181	264	-	547	719	19	52	-	24	5	450.01	-
Ni/Fe	176	256	396	566	731	18	50	20	7	6	152.06	-

a: Calculated from Gaussian deconvolution of NH_3-TPD profiles.

b: Mean particle size.

The profiles show that weak, low moderate and strong acid sites are present in all the samples while the moderate acid sites are observed in the Ni/Fe catalyst. Thus, it is possible to deduce that the third peak in the Ni/Fe catalyst is originated by the disappearance of Al. In addition, very strong acid sites are shown only in the Ni/Al_1Fe_1, Ni/Al_1Fe_3 and Ni/Fe. The fifth peak increases in intensity when the loading of Fe is higher. The decrease of the Al/Fe molar ratio predominantly decreases the strong acid sites (F4). The Ni/Al displayed 53% strength while Ni/Fe showed 7 %. In addition, the total amount of acid sites decreased from 891.65 to 152.06 μmol NH_3/g_{cat}, in accordance with the decrease of Al/Fe molar ratio.

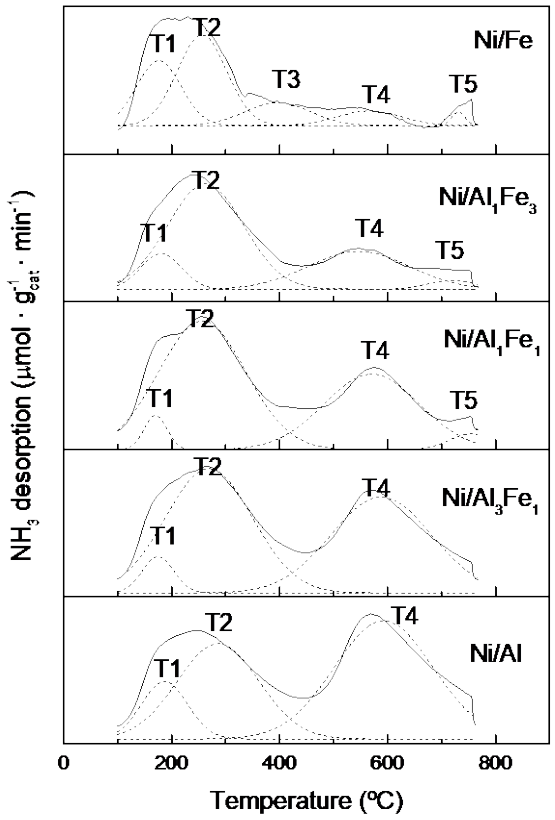

Fig. 7. NH_3-TPD profiles of the calcined catalysts.

The decrease in the total acidity when the Al/Fe molar ratio decreases is clear. The Ni/Al_3Fe_1 catalyst shows the highest glycerol conversion, carbon yield to gases and carbon yield to liquids. Moreover, this is the catalyst with the highest H_2 yield. This means that the combination of high acidity, interaction of metals (Ni, Al and Fe), small crystallite size and surface area stability produces high hydrogenation of acetol to 1,2-propanediol due to the presence of hydrogen in the reaction medium caused by the partial conversion of glycerol to gases. In contrast, the Ni/Fe catalyst presents the lowest total acidity with almost no conversion of glycerol to gases and the lowest glycerol conversion, which can explain the lack of hydrogenation of acetol to 1,2-propanediol. The absence of Ni-Al interactions and Ni-Al-Fe interactions could be the reason for the low catalytic activity of the Ni/Fe catalyst. The conversion of glycerol to liquid and gaseous products is required in order to obtain hydrogen that participates in the

hydrogenation of acetol to 1,2-propanediol, the desired product. The acidity and metal interaction of Ni-Al-Fe can play a significant role in the catalytic activity.

STEM images of the used catalysts and the metallic particle size distribution of the Ni/Al and Ni/Al_3Fe_1 catalysts are displayed in Fig. 8. The nickel-rich particle size of these samples is measured by image processing software, estimating mean diameter values of approximately 12.3 nm and 8.4 nm for the Ni/Al and Ni/Al_3Fe_1 catalysts, respectively. Around two hundred particles were measured per sample. It was not possible to obtain this nickel-rich particle size for the Ni/Al_1Fe_1, Ni/Al_1Fe_3 and Ni/Fe catalysts. This could be because these catalysts have plate-like particles and non-rigid aggregates, as was observed with the N_2 adsorption technique.

Although the particle sizes determined by STEM are slightly different from those determined by XRD, both techniques have shown the smallest particle size for the Ni/Al_3Fe_1 catalyst. This result indicates the highest dispersion of nickel in the Ni/Al_3Fe_1 catalyst and this could influence its catalytic performance.

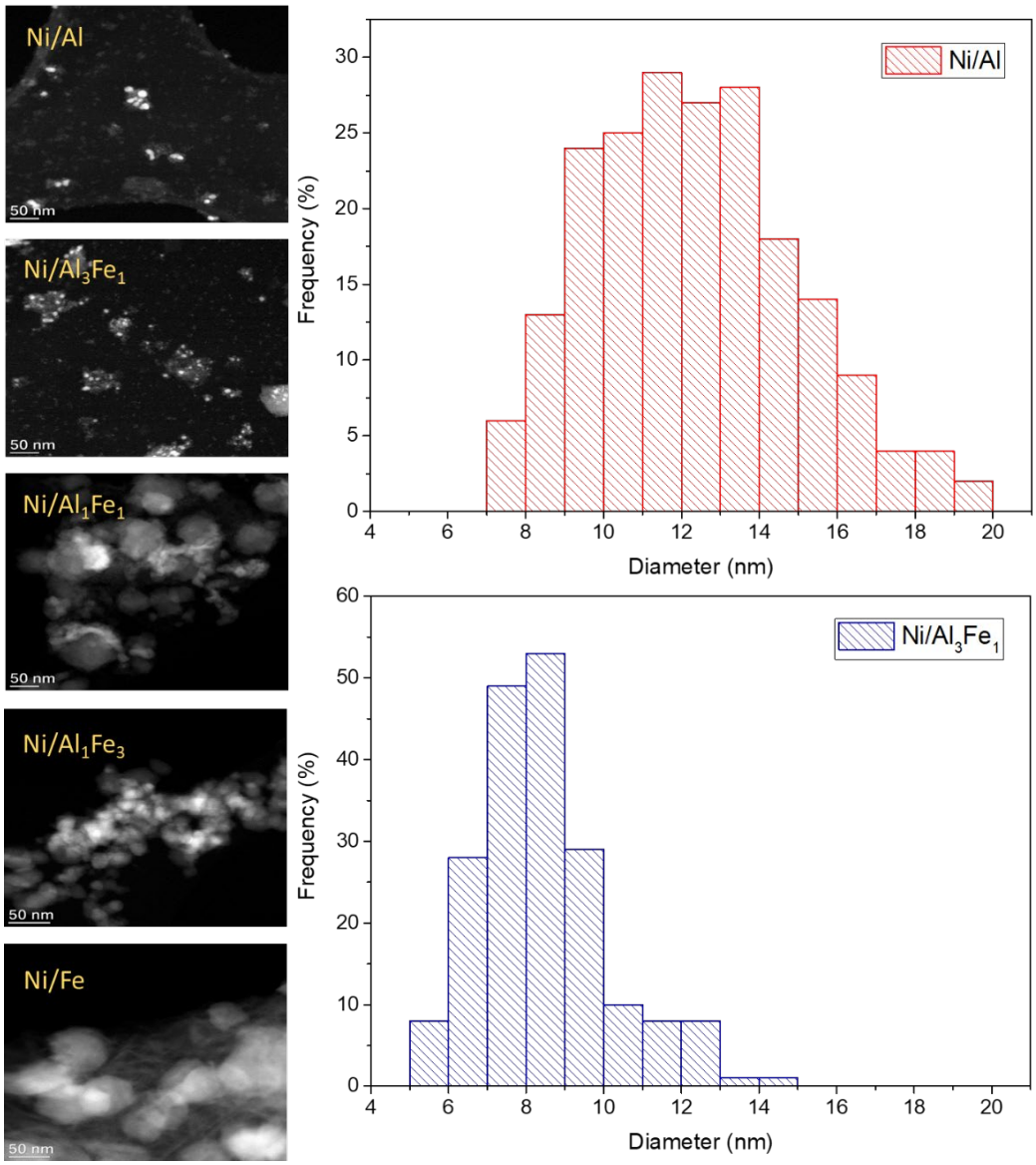

Fig. 8. STEM images of used catalysts and metal particle size distribution of Ni/Al and Ni/Al_3Fe_1 catalysts.

FESEM images of the catalysts (calcined and used) were taken in order to study the morphology of the samples, which are shown in Fig. 9. It is observed that the morphology of the catalysts changed after their use. Moreover, the FESEM images of the used catalysts (Ni/Al, Ni/Al_3Fe_1 and Ni/Al_1Fe_1) show the boehmite morphology, which was identified by the XRD technique. It was observed that the boehmite morphology changed with the variation of the Al content in the catalysts. Denigres et al. [49] reported that the boehmite morphology varies depending on the initial condition of

hydrothermal synthesis: being cubes, thick plates, elongated shapes or platelet-like particles.

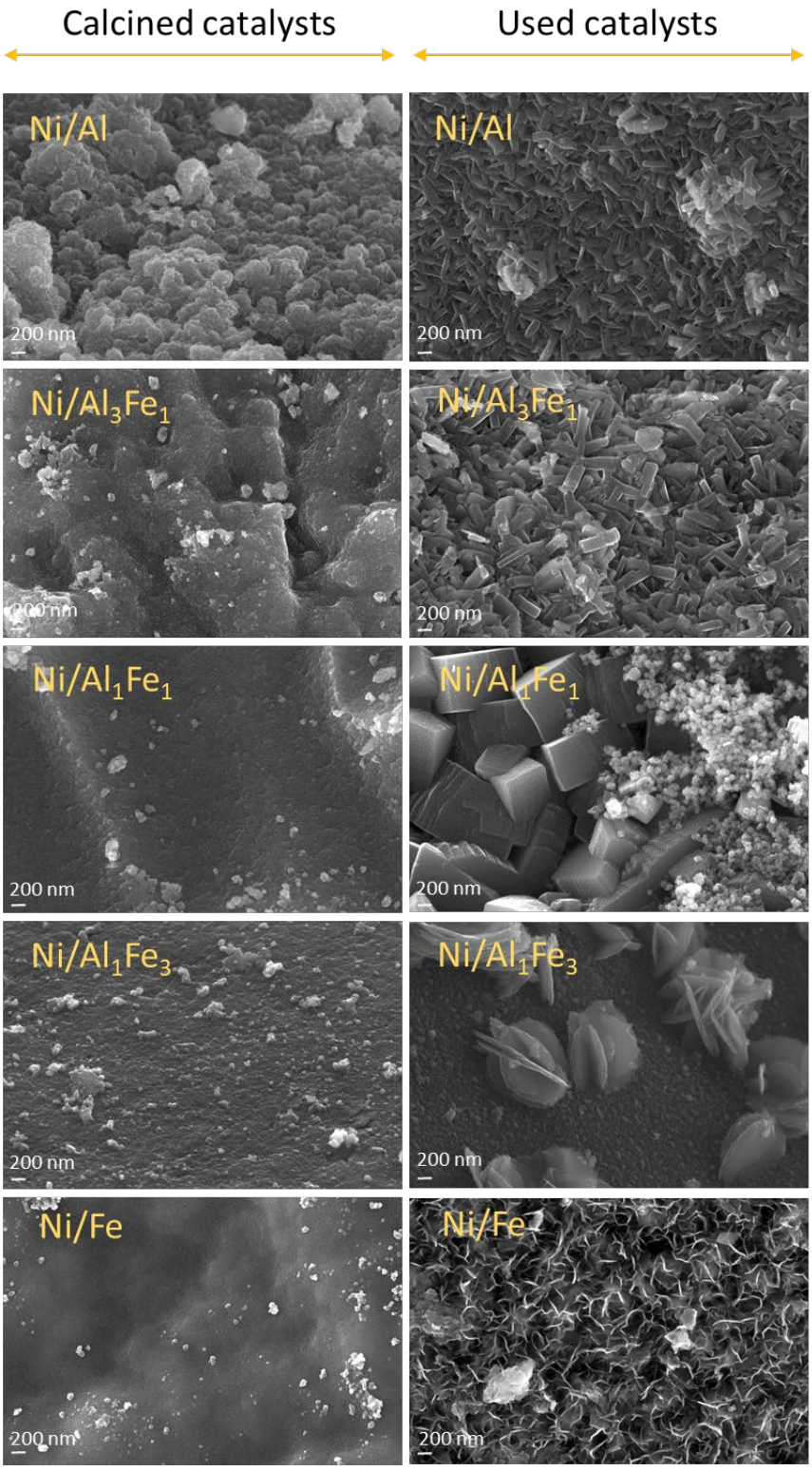

Fig. 9. FESEM images of calcined and used catalysts from left to right.

In addition, the morphology of the reduced Ni/Al_3Fe_1 catalyst, which presented the best performance in the APH of glycerol, was studied in order to analyse the influence of the reduction on the morphology of this catalyst. There are almost no differences between the morphology of the calcined and reduced catalyst (Fig. 10).

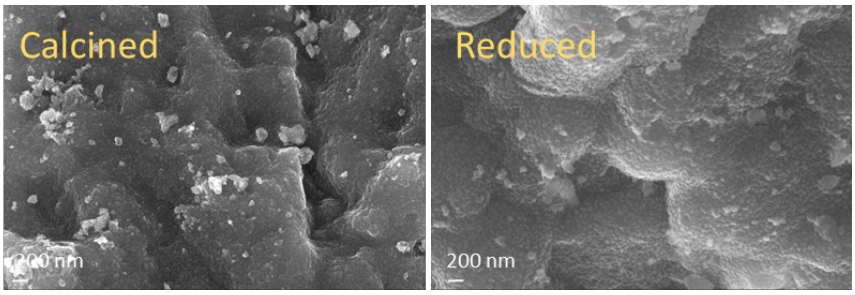

Fig. 10. FESEM images of calcined and reduced Ni/Al_3Fe_1 catalyst from left to right.

Additionally, elemental analysis of the spent catalysts was performed in order to determine the formation of coke. It was observed that the Ni/Al_3Fe_1, Ni/Al_1Fe_1 and Ni/Al_1Fe_3 catalysts present less coke formation expressed using the ratio mg $C/(g_{catalyst} \cdot g_{glycerol\ reacted})$ than the Ni/Al and Ni/Fe catalysts (Table 7). The catalysts with mixed oxide supports produced higher catalytic activity and less coke formation than the Ni/Al and Ni/Fe catalysts.

Table 7. Elemental analysis results of the used catalysts.

	C (wt.%)	H (wt.%)	Ratio mg $C/(g_{catalyst} \cdot g_{glycerol\ reacted})$
Ni/Al	3.70	1.53	8.76
Ni/Al_3Fe_1	3.78	1.61	5.22
Ni/Al_1Fe_1	3.13	1.09	5.42
Ni/Al_1Fe_3	2.61	0.65	4.91
Ni/Fe	2.01	0.49	38.94

4. Conclusions

Different Ni/Al-Fe catalysts synthesized by co-precipitation, changing the molar ratio of Al/Fe and their physicochemical characteristics, were studied. The decrease of the Al/Fe molar ratio reduced the surface area values, the Ni/Al_3Fe_1 catalyst showing the least reduction but an increase in the average pore diameter. This catalyst had considerable morphology stability despite the severe hydrothermal conditions it suffered during the reaction, and it had the smallest crystallite size. Furthermore, the increase in the Fe content in the catalyst reduced the formation of boehmite and favoured the Ni reducibility at low temperatures. The increase in the Fe content and the decrease in the Al content diminished the strong acid sites and the total number of acid sites. High interaction between metals were detected with phases such as $FeNi_3$, $AlNi_3$ and Ni-Fe alloys. The mixed oxide supports produced higher catalytic activity and less coke formation than the Ni/Al and Ni/Fe catalysts.

The Ni/Al_3Fe_1 catalyst showed the maximum glycerol conversion (42.31 %), carbon yield to gases (6.57 %) and carbon yield to liquids (30.45%). 1,2-propanediol was the value-added product with the highest carbon selectivity (70.89%). The catalytic activity decreased in the following order: $Ni/Al_3Fe_1 > Ni/Al_1Fe_1 > Ni/Al_1Fe_3 > Ni/Al > Ni/Fe$. The presence of $FeNi_3$ phase in the catalysts could favour the hydrogenation of acetol to 1,2-propanediol and the glycerol conversion. Conversely, the Ni-Fe alloys (taenite and kamacite) do not favour the APH of glycerol.

Acknowledgments

The authors wish to express their gratitude to the AEI/FEDER, UE (project CTQ2017-86893-R) for providing financial support for the work. The authors acknowledge the funding from the Aragón Government (ref. T22_20R), co-funded by FEDER 2014-2020 "Construyendo Europa desde Aragón". The authors would also like to acknowledge the use of the Servicio General de Apoyo a la Investigación-SAI of the Universidad de Zaragoza.

References

[1] T. Mahlia, Z. Syazmi, M. Mofijur, A. Abas, M. Bilad, H. Ong, A. Silitonga, Patent landscape review on biodiesel production: Technology updates, Renewable & Sustainable Energy Reviews, 118 (2020).

[2] M.K. Awasthi, S. Sarsaiya, A. Patel, A. Juneja, R.P. Singh, B. Yan, S.K. Awasthi, A. Jain, T. Liu, Y. Duan, A. Pandey, Z. Zhang, M.J. Taherzadeh, Refining biomass residues for sustainable energy and bio-products: An assessment of technology, its importance, and strategic applications in circular bio-economy, Renewable and Sustainable Energy Reviews, 127 (2020) 109876.

[3] C. Quispe, C. Coronado, J. Carvalho, Glycerol: Production, consumption, prices, characterization and new trends in combustion, Renewable & Sustainable Energy Reviews, 27 (2013) 475-493.

[4] S. Chozhavendhan, M.V.P. Singh, B. Fransila, R.P. Kumar, G.K. Devi, A review on influencing parameters of biodiesel production and purification processes, Current Research in Green and Sustainable Chemistry, 1-2 (2020) 1-6.

[5] J. Remon, J. Gimenez, A. Valiente, L. Garcia, J. Arauzo, Production of gaseous and liquid chemicals by aqueous phase reforming of crude glycerol: Influence of operating conditions on the process, Energy Conversion and Management, 110 (2016) 90-112.

[6] C. Zhou, H. Zhao, D. Tong, L. Wu, W. Yu, Recent Advances in Catalytic Conversion of Glycerol, Catalysis Reviews-Science and Engineering, 55 (2013) 369-453.

[7] A. Morales-Marin, J. Ayastuy, U. Iriarte-Velasco, M. Gutierrez-Ortiz, C.T. Environm, Nickel aluminate spinel-derived catalysts for the aqueous phase reforming of glycerol: Effect of reduction temperature, Applied Catalysis B-Environmental, 244 (2019) 931-945.

[8] S. Zhu, X. Gao, Y. Zhu, H. Zheng, Y. Li, Promoting effect of boron oxide on Cu/SiO_2 catalyst for glycerol hydrogenolysis to 1,2-propanediol, Journal of Catalysis, 303 (2013) 70-79.

[9] A. Martin, U. Armbruster, I. Gandarias, P. Arias, Glycerol hydrogenolysis into propanediols using in situ generated hydrogen - A critical review, European Journal of Lipid Science and Technology, 115 (2013) 9-27.

[10] M. Monteiro, C. Kugelmeier, R. Pinheiro, M. Batalha, A. Cesar, Glycerol from biodiesel production: Technological paths for sustainability, Renewable & Sustainable Energy Reviews, 88 (2018) 109-122.

[11] T. Werpy, G. Petersen, Top Value Added Chemicals from Biomass: Volume I - Results of Screening for Potencial Candidates from Sugars and Synthesis Gas, US Department of Energy (US), United States, 2004.

[12] N. Pandhare, S. Pudi, P. Biswas, S. Sinha, Vapor phase hydrogenolysis of glycerol to 1,2-propanediol over gamma-Al2O3 supported copper or nickel monometallic and copper-nickel bimetallic catalysts, Journal of the Taiwan Institute of Chemical Engineers, 61 (2016) 90-96.

[13] F. Cai, D. Pan, J. Ibrahim, J. Zhang, G. Xiao, Hydrogenolysis of glycerol over supported bimetallic Ni/Cu catalysts with and without external hydrogen addition in a fixed-bed flow reactor, Applied Catalysis a-General, 564 (2018) 172-182.

[14] V. Yfanti, E. Vasiliadou, S. Sklari, A. Lemonidou, Hydrodeoxygenation of glycerol with in situ H-2 formation over Pt catalysts supported on Fe modified Al2O3: effect of Fe loading, Journal of Chemical Technology and Biotechnology, 92 (2017) 2236-2245.

[15] M. Dasari, P. Kiatsimkul, W. Sutterlin, G. Suppes, Low-pressure hydrogenolysis of glycerol to propylene glycol, Applied Catalysis a-General, 281 (2005) 225-231.

[16] L. Garcia, A. Valiente, M. Oliva, J. Ruiz, J. Arauzo, Influence of operating variables on the aqueous-phase reforming of glycerol over a Ni/Al coprecipitated catalyst, International Journal of Hydrogen Energy, 43 (2018) 20392-20407.

[17] M.H. Mohamad, R. Awang, W.M.Z.W. Yunus, A Review of Acetol: Application and Production, American Journal of Applied Sciences, 11 (2011) 1135-1139.

[18] A. Soares, H. Atia, U. Armbruster, F. Passos, A. Martin, Platinum, palladium and nickel supported on Fe3O4 as catalysts for glycerol aqueous-phase hydrogenolysis and reforming, Applied Catalysis a-General, 548 (2017) 179-190.

[19] D. Roy, B. Subramaniam, R. Chaudhari, Aqueous phase hydrogenolysis of glycerol to 1,2-propanediol without external hydrogen addition, Catalysis Today, 156 (2010) 31-37.

[20] F. Bossola, X. Pereira-Hernandez, C. Evangelisti, Y. Wang, V. Dal Santo, Investigation of the promoting effect of Mn on a Pt/C catalyst for the steam and aqueous phase reforming of glycerol, Journal of Catalysis, 349 (2017) 75-83.

[21] J. Callison, N. Subramanian, S. Rogers, A. Chutia, D. Gianolio, C. Catlow, P. Wells, N. Dimitratos, Directed aqueous-phase reforming of glycerol through tailored platinum nanoparticles, Applied Catalysis B-Environmental, 238 (2018) 618-628.

[22] W. Zhou, Y. Zhao, S. Wang, X. Ma, The effect of metal properties on the reaction routes of glycerol hydrogenolysis over platinum and ruthenium catalysts, Catalysis Today, 298 (2017) 2-8.

[23] E. Maris, R. Davis, Hydrogenolysis of glycerol over carbon-supported Ru and Pt catalysts, Journal of Catalysis, 249 (2007) 328-337.

[24] Y. Shinmi, S. Koso, T. Kubota, Y. Nakagawa, K. Tomishige, Modification of Rh/SiO2 catalyst for the hydrogenolysis of glycerol in water, Applied Catalysis B-Environmental, 94 (2010) 318-326.

[25] R. Chimentao, B. Miranda, D. Ruiz, F. Gispert-Guirado, F. Medina, J. Llorca, J. Santos, Catalytic performance of zinc-supported copper and nickel catalysts in the glycerol hydrogenolysis, Journal of Energy Chemistry, 42 (2020) 185-194.

[26] B. Miranda, R. Chimentao, J. Santos, F. Gispert-Guirado, J. Llorca, F. Medina, F. Bonillo, J. Sueiras, Conversion of glycerol over 10%Ni/gamma-Al2O3 catalyst, Applied Catalysis B-Environmental, 147 (2014) 464-480.

[27] A. Seretis, P. Tsiakaras, Hydrogenolysis of glycerol to propylene glycol by in situ produced hydrogen from aqueous phase reforming of glycerol over SiO2-Al2O3 supported nickel catalyst, Fuel Processing Technology, 142 (2016) 135-146.

[28] F. Bastan, M. Kazemeini, A. Larimi, H. Maleki, Production of renewable hydrogen through aqueous-phase reforming of glycerol over Ni/Al2O3-MgO nano-catalyst, International Journal of Hydrogen Energy, 43 (2018) 614-621.

[29] M. El Doukkali, A. Iriondo, N. Miletic, J. Cambra, P. Arias, Hydrothermal stability improvement of NiPt-containing gamma-Al2O3 catalysts tested in aqueous phase reforming of glycerol/water mixture for H-2 production, International Journal of Hydrogen Energy, 42 (2017) 23617-23630.

[30] R. Manfro, A. da Costa, N. Ribeiro, M. Souza, Hydrogen production by aqueous-phase reforming of glycerol over nickel catalysts supported on CeO2, Fuel Processing Technology, 92 (2011) 330-335.

[31] A. Reynoso, J. Ayastuy, U. Iriarte-Velasco, M. Gutierrez-Ortiz, C.T. Environm, Cobalt aluminate spinel-derived catalysts for glycerol aqueous phase reforming, Applied Catalysis B-Environmental, 239 (2018) 86-101.

[32] A. Kant, Y. He, A. Jawad, X. Li, F. Rezaei, J. Smith, A. Rownaghi, Hydrogenolysis of glycerol over Ni, Cu, Zn, and Zr supported on H-beta, Chemical Engineering Journal, 317 (2017) 1-8.

[33] J. Remon, C. Jarauta-Cordoba, L. Garcia, J. Arauzo, Effect of acid (CH3COOH, H2SO4 and H3PO4) and basic (KOH and NaOH) impurities on glycerol valorisation by aqueous phase reforming, Applied Catalysis B-Environmental, 219 (2017) 362-371.

[34] I. Freitas, R. Manfro, M. Souza, Hydrogenolysis of glycerol to propylene glycol in continuous system without hydrogen addition over Cu-Ni catalysts, Applied Catalysis B-Environmental, 220 (2018) 31-41.

[35] A. Soares, G. Perez, F. Passos, Alumina supported bimetallic Pt-Fe catalysts applied to glycerol hydrogenolysis and aqueous phase reforming, Applied Catalysis B-Environmental, 185 (2016) 77-87.

[36] I. Jimenez-Morales, F. Vila, R. Mariscal, A. Jimenez-Lopez, Hydrogenolysis of glycerol to obtain 1,2-propanediol on Ce-promoted Ni/SBA-15 catalysts, Applied Catalysis B-Environmental, 117 (2012) 253-259.

[37] G. Wang, Y. Jin, G. Liu, Y. Li, Production of Hydrogen and Nanocarbon from Catalytic Decomposition of Methane over a Ni-Fe/Al2O3 Catalyst, Energy & Fuels, 27 (2013) 4448-4456.

[38] F. Meng, P. Zhong, Z. Li, X. Cui, H. Zheng, Surface Structure and Catalytic Performance of Ni-Fe Catalyst for Low-Temperature CO Hydrogenation, Journal of Chemistry, (2014).

[39] J.F. Blais, Z. Djedidi, R.B. Cheikh, R.D. Tyagi, G. Mercier, Metals Precipitation from Effluents: Review, Practice periodical of hazardous, toxic, and radioactive waste management, 12 (2008) 135-149.

[40] M. Thommes, K. Kaneko, A. Neimark, J. Olivier, F. Rodriguez-Reinoso, J. Rouquerol, K. Sing, Physisorption of gases, with special reference to the evaluation of surface area and pore size distribution (IUPAC Technical Report), Pure and Applied Chemistry, 87 (2015) 1051-1069.

[41] C. Garcia-Sancho, R. Guil-Lopez, A. Sebastian-Lopez, R. Navarro, J. Fierro, Hydrogen production by methane decomposition: A comparative study of supported and bulk ex-hydrotalcite mixed oxide catalysts with Ni, Mg and Al, International Journal of Hydrogen Energy, 43 (2018) 9607-9621.

[42] L. ALZAMORA, J. ROSS, E. KRUISSINK, L. VANREIJEN, COPRECIPITATED NICKEL-ALUMINA CATALYSTS FOR METHANATION AT HIGH-TEMPERATURE .2. VARIATION OF TOTAL AND METALLIC AREAS AS A FUNCTION OF SAMPLE COMPOSITION AND METHOD OF PRETREATMENT, Journal of the Chemical Society-Faraday Transactions I, 77 (1981) 665-681.

[43] F. Muniz, M. Miranda, C. dos Santos, J. Sasaki, The Scherrer equation and the dynamical theory of X-ray diffraction, Acta Crystallographica a-Foundation and Advances, 72 (2016) 385-390.

[44] V. Uvarov, I. Popov, Metrological characterization of X-ray diffraction methods at different acquisition geometries for determination of crystallite size in nano-scale materials, Materials Characterization, 85 (2013) 111-123.

[45] D. Shi, R. Wojcieszak, S. Paul, E. Marceau, Ni Promotion by Fe: What Benefits for Catalytic Hydrogenation?, Catalysts, 9 (2019).

[46] B. Li, Y. Luo, B. Li, X. Yuan, X. Wang, Catalytic performance of iron-promoted nickel-based ordered mesoporous alumina FeNiAl catalysts in dry reforming of methane, Fuel Processing Technology, 193 (2019) 348-360.

[47] K. Kim, B. Kwak, N. Park, T. Lee, S. Lee, M. Kang, Effective hydrogen production from propane steam reforming over bimetallic co-doped NiFe/Al2O3 catalyst, Journal of Industrial and Engineering Chemistry, 46 (2017) 324-336.

[48] A.C.P. Borges, J.A. Onwundili, H. Andrade, C. Alves, A. Ingram, S. Vieira de Melo, E. Torres, Catalytic Properties and Recycling of NiFe2O4 Catalyst for Hydrogen Production by Supercritical Water Gasification of Eucalyptus Wood Chips, Energies, 13 (2020) 4553.

[49] R. Denigres, G. Rocha, C. Montes, A. Vieira-Coelho, Synthesis and Characterization of Boehmites Obtained from Gibbsite in Presence of Different Environments, Materials Research-Ibero-American Journal of Materials, 19 (2016) 659-668.